

The ITER core imaging x-ray spectrometer

P Beiersdorfer¹, J Clementson¹, J Dunn¹, M F Gu^{1,4}, K Morris¹,
Y Podpaly^{1,5}, E Wang¹, M Bitter², R Feder², K W Hill², D Johnson²
and R Barnsley³

¹ Lawrence Livermore National Laboratory, Livermore, CA 94550, USA

² Princeton Plasma Physics Laboratory, Princeton, NJ 08543, USA

³ ITER Cadarache JWS, Cadarache Centre, 13108 St Paul-Les-Durance, France

E-mail: beiersdorfer@llnl.gov

Received 29 November 2009, in final form 17 February 2010

Published 5 July 2010

Online at stacks.iop.org/JPhysB/43/144008

Abstract

The core imaging x-ray spectrometer (CIXS) is one of several ITER diagnostic systems planned for measurements of the central ion and electron temperature profiles and of the toroidal and poloidal rotation velocity profiles, T_i , T_e , v_ϕ , and v_θ respectively. The diagnostic is based on precision determinations of the Doppler broadening and centroid shift of the lines of highly ionized heavy impurities using a curved Bragg crystal spectral disperser and imager. In a departure from earlier designs, the CIXS employs a novel imaging geometry utilizing spherically bent crystals operating at a Bragg angle near 45° , which spatially and spectrally resolves the x-ray emission from the plasma. In addition, the working radiation will be the L-shell emission of highly charged tungsten ions. Particular emphasis is placed on the strong $3d_{5/2} \rightarrow 2p_{3/2}$ electric dipole transition in neon-like tungsten W^{64+} . Here we present the conceptual design of the instrument, which may include an x-ray calorimeter, and discuss the spectral features used in future measurements.

(Some figures in this article are in colour only in the electronic version)

1. Introduction

X-ray spectroscopy of high-temperature plasmas provides a wealth of information, including elemental content, electron temperature, electron density, ion motion, and ionization fraction, which often cannot be inferred by other means. In high-energy astronomy, x-ray spectroscopy has been an indispensable tool for studying such varied objects as stellar coronae, active galactic nuclei, and clusters of galaxies [1]. X-ray spectroscopy is also one of the principal diagnostics of magnetic fusion plasmas [2, 3] ever since the first studies found an enhanced x-ray radiation in excess of the level expected from a pure hydrogen plasma [4].

Crystal spectroscopy for ion temperature measurements of magnetically confined fusion plasmas has been pioneered

by Bitter *et al.*, who first studied the broadening of the $1s2p\ ^1P_1 \rightarrow 1s^2\ ^1S_0$ resonance line in helium-like Fe^{24+} on the Princeton Large Torus (PLT) tokamak [5]. Crystal spectrometers were subsequently used on a variety of magnetic fusion machines, such as Alcator, the Tokamak Fusion Test Reactor (TFTR), the Tokamak Fontenay aux Roses (TFR), the Joint European Torus (JET), Tore Supra, the Axially Symmetric Divertor Experiment (ASDEX), and Doublet III [6–14]. The instruments usually studied the emission from helium-like or hydrogen-like ions and had a single line of sight. The sight line was typically along a radial chord in the midplane of the plasma. This arrangement provided the ion temperature at the centre of the machine, i.e. from the hottest part of the plasma where the helium-like or hydrogen-like ion species under study was produced and predominantly excited. In order to obtain measurement points at different radial locations, multiple instruments were constructed, each viewing the plasma at a different tangency radius and thus

⁴ Present address: Space Sciences Laboratory, University of California, Berkeley, CA 94720, USA.

⁵ Permanent address: Plasma Science and Fusion Center, Massachusetts Institute of Technology, Cambridge, MA 02139, USA.

providing a different radial point for each line of sight [15, 16].

The need for multiple instruments limited the utility of crystal spectrometers for obtaining radial profiles of the ion temperature. As a result, ion temperature profile measurements have been made instead on many machines by charge exchange recombination spectroscopy, which radially probes the plasma ion temperature with the aid of a diagnostic neutral beam [17]. The implementation of charge exchange recombination spectroscopy on ITER, however, is difficult [18, 19]. The reason is that the neutral beam cannot readily penetrate the very large, hot plasma volume of ITER. As a result, the signal from the plasma core is attenuated, while the background from the intervening plasma is enhanced. A charge exchange recombination spectroscopy system is planned for ITER. However, its primary purpose will be the measurement of the helium ash accumulation in ITER plasmas [20, 21]. Crystal spectroscopy is, therefore, considered to be the primary diagnostic for measuring the core ion temperature in ITER [22].

Early crystal spectrometer designs envisioned the need for up to 16 lines of sight to cover the ITER plasma [23]. This design was simplified more recently [24] by making use of a new type of imaging geometry that had been proposed by Bitter *et al* [25]. The new geometry allows the use of a single crystal spectrometer to image the plasma and thus to provide radial profiles of the ion temperature with high spatial resolution. Because ITER's plasmas are much hotter than those of current magnetic confinement devices, the most recent design of the ITER crystal spectrometer for measuring the core ion temperature [24] utilized the emission of helium-like krypton, which is predicted to exist at the 15–25 keV electron temperatures expected in the core of ITER.

In the past few years the United States has commenced an effort in the conceptual design of the ITER core imaging x-ray spectrometer (CIXS), and a team consisting of scientists and engineers from the Lawrence Livermore National Laboratory and the Princeton Plasma Physics Laboratory has revisited the earlier design. In addition to adopting the new imaging geometry, a major change was made by shifting away from the K-shell spectrum of helium-like krypton to the L-shell spectrum of neon-like tungsten. An important aspect of the conceptual design has been the integration of the CIXS into equatorial port plug number 9. Here, the CIXS shares space with the US Electron Cyclotron Emission diagnostic, the US Toroidal Interferometer Polarimeter diagnostic, and the EU Visible/IR Imaging System. The resulting design of the CIXS provides several tomographic views of the central ITER plasma for determining the central ion temperature profile. In addition, it can provide information on the ionization balance, impurity concentration, the electron temperature, and on the bulk ion motion.

The paper is organized as follows. We first give a brief introduction to the ITER plasma environment relevant to the design of the CIXS. This is followed by a description of the imaging properties of bent crystal spectrometers. Subsequently we discuss the atomic physics criteria for selecting the L-shell tungsten emission as the working

radiation of the CIXS and present some of the few available laboratory data on neon-like W^{64+} . We then proceed to present the layout of the instrument on ITER. In the concluding section we point out some of the outstanding issues and discuss the advantages for including an x-ray calorimeter in the design of the CIXS.

2. The ITER plasma environment

The volume of ITER's plasma will greatly exceed that of any magnetic fusion device ever built, as illustrated in figure 1. The plasma's major radius is 6.2 m, and the minor radius is 2 m. The total volume thus is 840 m³. This compares to 12.5 m³ for the National Spherical Torus Experiment (NSTX), 30 m³ for the Large Helical Device (LHD), and 35 m³ for TFTR. The largest two magnetic fusion devices operating at present, the JT-60 tokamak and JET, have a plasma volume of about 100 m³.

The temperature of ITER's plasma core is expected by design to achieve values of 20 to 30 keV. A typical ion and electron temperature profile predicted for one of the ITER performance scenarios is shown in figure 2 [26]. The time evolution of the average ITER plasma temperature is shown in figure 3. This figure also shows the presumed power input. The average electron density is thought to approach values of 10¹⁴ cm⁻³.

ITER plasmas are designed to have an effective charge Z_{eff} close to unity. Most likely, $Z_{\text{eff}} \approx 1.4$ –1.8. The only element with high atomic number Z likely to be found indigenously in the plasma is tungsten [27, 28]. Tungsten is the material of choice for plasma-facing components, as it has a high melting point, low sputtering yield and small retention of tritium. Tungsten is considered in particular for the divertor, as shown in figure 4. Current predictions are that the tungsten concentration may reach one part in 10⁻⁵ or higher in the plasma. For comparison, the concentration of beryllium, which is used throughout most of the vacuum vessel, may be 2 parts in 10⁻², that of carbon may be 1 part in 10⁻², and that of argon, which may be used to radiatively cool the divertor, may be 1 part in 10⁻³ [29].

If the indigenous amount of tungsten in ITER plasmas would suffice to diagnose the central ion temperature, then there would be no need for further impurity enrichment with high- Z elements such as krypton. This is important, as any impurity, especially any high- Z impurity, would contribute to the radiative losses and thus cool the plasma and make ignition and burn more difficult. The fact that tungsten is indigenous to ITER plasma is one of the major reasons we have selected tungsten radiation as the 'working medium' of the CIXS diagnostic.

A burning ITER plasma will be a tremendous source of neutrons. The neutron flux is expected to be around 10¹⁸ s⁻¹ m⁻². Electronic equipment typically is sensitive to neutrons and can be damaged when a certain dose level is exceeded. This is also true for the x-ray detectors that are part of the CIXS. Shielding will be needed, which means that a detector is ideally located as far away from the plasma as possible so that the most material can be placed between it and the plasma.

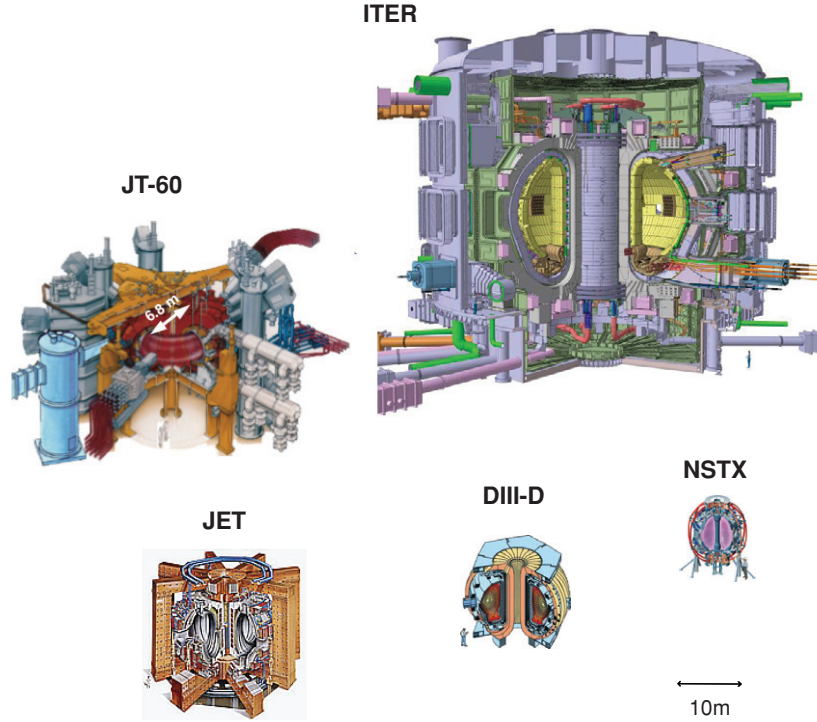


Figure 1. The ITER machine and comparison with other current magnetically confined plasma devices: the JT-60 tokamak (Japan), JET (EU), the DIII-D tokamak (US), and NSTX (US).

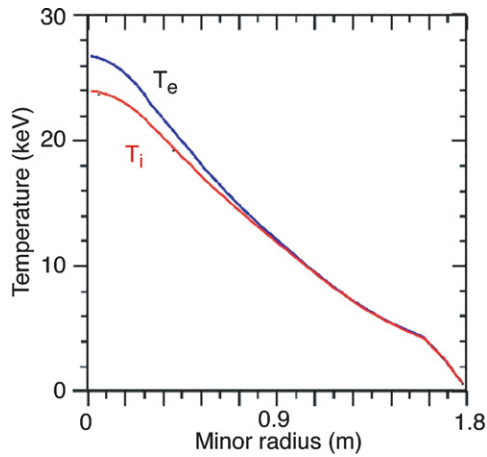


Figure 2. Radial electron and ion temperature profiles of typical ITER plasmas. Figure adapted from [26].

3. Imaging properties of the ITER bent-crystal spectrometer

Bent-crystal spectrometers have been the instruments of choice to measure the central ion temperature on many magnetic fusion devices. The bent-crystal geometry greatly increases the x-ray flux that can be recorded over that observed with a flat-crystal spectrometer, which is true for both the Johann and the von Hámós geometry [30, 31]. Moreover, the Johann geometry does not require an entrance slit, and the reflection of the entire crystal contributes to the intensity of a given x-ray line.

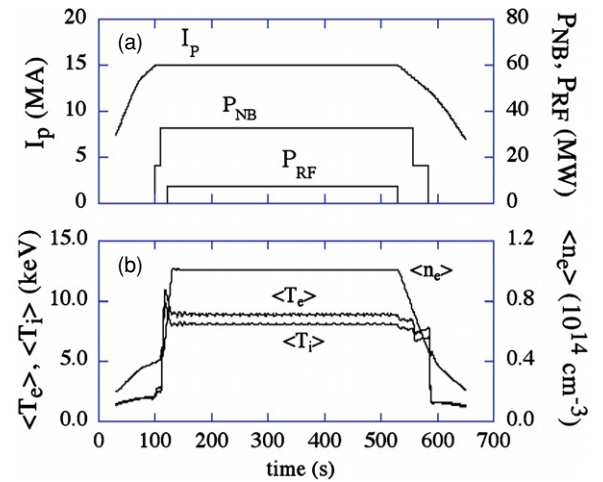


Figure 3. Time evolution of plasma parameters: (a) plasma current (I_p), heating power from neutral beam injection (P_{NB}) and radio-frequency wave injection (P_{RF}); (b) spatially averaged electron temperature (T_e), ion temperature (T_i) and electron density (n_e). Figure adapted from [26].

A schematic of the focusing properties of the Johann geometry is shown in figure 5. The crystal, which is cylindrically bent about an axis out of the page, diffracts x-rays with wavelength λ according to Bragg's law

$$n\lambda = 2d \sin \theta, \quad (1)$$

where n is the order of diffraction, d is the lattice spacing of the crystal and θ is the angle of diffraction, i.e. the Bragg angle. For a crystal bent to a radius of curvature R_c , x-rays of a given

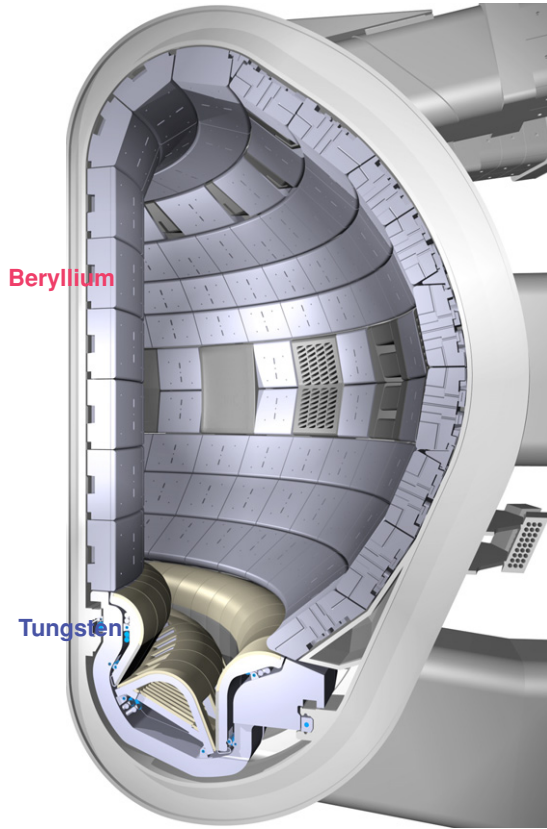


Figure 4. In-vessel view of ITER showing beryllium tiles in the main chamber and tungsten tiles in the divertor region.

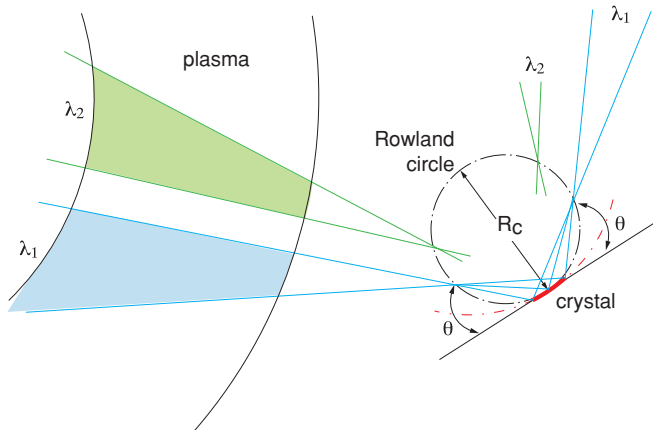


Figure 5. Focusing properties of the Johann geometry. The Johann geometry employs a cylindrically bent crystal with radius R_c to focus x-rays of wavelength λ on to a circle with radius $R_c/2$, the so-called Rowland circle. According to Bragg's law x-rays of different wavelengths are focused on different points along the Rowland circle and stem from different parts of the plasma.

wavelength are focused to a point on a circle of radius $R_c/2$. This circle is called the Rowland circle. The Rowland circle is tangent to the crystal, and the distance f_m from the centre of the crystal to the focal point is given by

$$f_m = R_c \sin \theta. \quad (2)$$

X-rays with a different wavelength are focused at a different point along the Rowland circle and come from a different part of the plasma, as illustrated in figure 5.

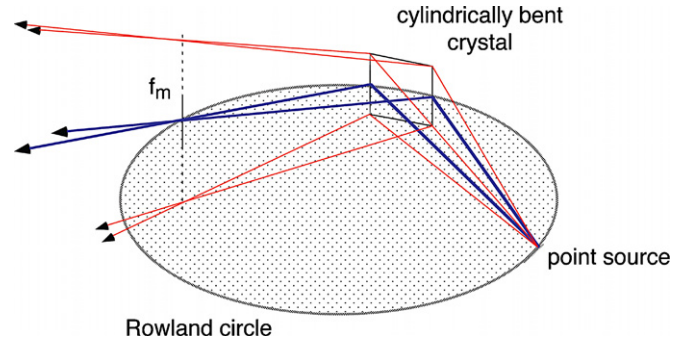


Figure 6. Focusing properties of a cylindrically bent crystal illustrating the divergence of sagittal rays.

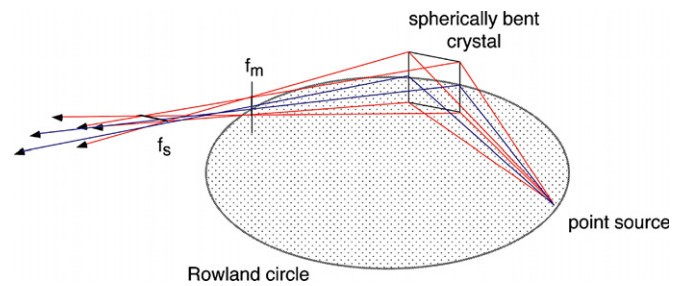


Figure 7. Focusing properties of a spherically bent crystal illustrating the focusing of sagittal rays.

The Johann geometry provides focusing only for the meridional rays, i.e. rays parallel to the diffraction plane, while the sagittal rays, which are oblique to the diffraction plane, are not focused. This is illustrated in figure 6. The sagittal rays can be focused, if a spherically bent crystal is used, as illustrated in figure 7. The focus of the sagittal rays f_s and the focus of the meridional rays f_m do not coincide. They are, however, related by the equation

$$f_s = -f_m / \cos(2\theta). \quad (3)$$

This means that focusing of the sagittal rays is only achieved, if the Bragg angle is larger than 45° . For $\theta = 45^\circ$ the sagittal are parallel, i.e. their focus is at infinity. For $\theta < 45^\circ$ the rays diverge, and the rays seem to emerge from a virtual sagittal focus behind the crystal.

The spherical crystal geometry can be used to obtain spatial imaging of the plasma, as described by Bitter *et al* [25]. For $\theta = 45^\circ$ the spatial resolution equals the width of the parallel bundle of rays, which in turn equals the height of the crystal. The divergence or convergence of the sagittal rays does not greatly change the spatial resolution given by the height of the crystal for small changes in θ , if a range of angles around 45° is used for spatial imaging.

The utility of spherically bent crystals for plasma imaging has been demonstrated on the Alcator C-Mod tokamak [32, 33]. There, the K-shell radiation of both Ar^{16+} and Ar^{17+} was used to produce temporally resolved radial profiles of the ion temperature and toroidal ion bulk velocities. The Bragg angles in these cases were about 61° and 55° .

For ITER we also plan to employ a spherically bent crystal. In order to bring the detector as far back to the wall of the equatorial port plug as possible, we need a Bragg angle

of 45° or less. In fact, for $\theta = 45^\circ$, the spectrometer layout would be ‘L’ shaped, which means that both the crystal and the detector can be situated along the back wall. For $\theta < 45^\circ$, the crystal moves forward, but the detector can still be situated at the back wall. For angles larger than 45° only the crystal can be placed near the back wall, and the detector has to move forward. As we have already mentioned, a Bragg angle of 45° is also ideal for spatial imaging. Consequently, we have selected a geometry that utilizes a Bragg angle close to 45° for our conceptual design.

The width of the equatorial port plug is somewhat over 1 m. As a result, we choose the distance between the crystal and the detector $f_m = 1$ m so that for a Bragg angle of 45° this choice means that $R_c = 1.41$ m.

Placement of the crystal at the back wall, which is about 5 m away from the plasma centre, means that the plasma will be demagnified by a factor of 5:1. The 2 m minor radius plasma can thus in principle be imaged on to a 40 cm tall detector. A spatial resolution of one part in 30 thus means that the height of the crystal should be about 13 mm.

The spectral resolving power $\lambda/\Delta\lambda$, which is critical for measuring the line shape, broadening and position of a given spectral line and thus the ion temperature and ion velocity, is given by

$$\frac{\lambda}{\Delta\lambda} = \frac{1}{\Delta\theta} \tan \theta. \quad (4)$$

The value of $\Delta\theta$ derives from the Johann error, which is given by

$$\Delta\theta = \frac{l_c^2}{8R_c^2 \tan \theta}. \quad (5)$$

Here l_c is the length of the crystal. For $l_c = 5$ cm, $\lambda/\Delta\lambda = 6400$. This is twice the minimum value needed for inferring the temperature from the broadening of an iron K-shell line at a temperature of 1 keV.

4. Choice of working radiation

At central electron temperatures of 20–40 keV the K-shell ions, such as Ar^{16+} , Cr^{22+} , Fe^{24+} and Ni^{26+} that have provided the working radiation of the crystal spectrometers on past and present-day machines, burn out and no longer emit K-shell x-rays. Barnsley *et al* [24], therefore, proposed using the radiation of helium-like Kr^{34+} as the working radiation of the ITER crystal spectrometer. Kr^{34+} ions exist between roughly 6 and 30 keV.

In preparation for ITER, early studies on the K-shell emission of krypton have been made at the SuperEBIT electron beam ion trap at Livermore [34–36] and the TFTR tokamak [37, 38]. The latter set of measurements have established the lower limit of electron temperature (≈ 6 keV) and profile width needed to produce K-shell radiation from krypton.

Krypton, however, does not occur naturally in ITER plasmas and must be introduced. This would increase the effective charge, Z_{eff} , of the plasma and may lead to a deleterious increase in the radiation losses [29]. By contrast, tungsten is expected to be an indigenous trace element in ITER plasmas, owing to the fact that the divertor includes tungsten

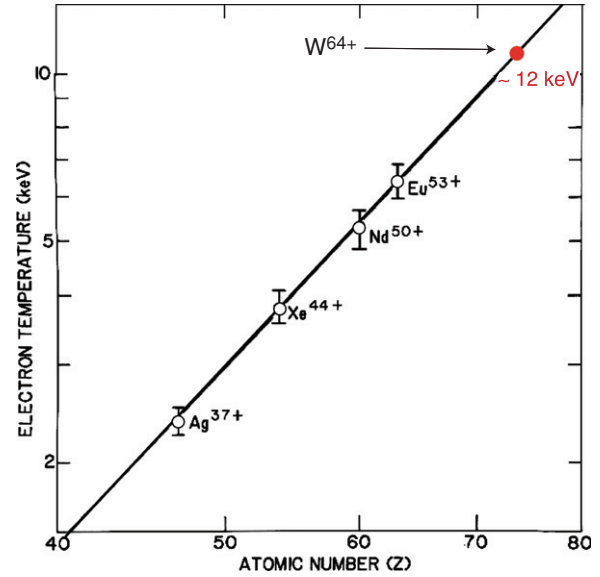


Figure 8. Threshold electron temperature for observing the x-ray emission of a given neon-like ion in PLT tokamak plasmas. Figure adapted from [40]. Extrapolation to neon-like tungsten suggests that a minimum temperature of 12 keV is needed.

as a plasma-facing component, as we already have discussed above.

The temperature in ITER will not be sufficient to strip tungsten to the helium-like charge state. Instead tungsten is likely to be found in the neon-like charge state, W^{64+} . Similar to helium-like ions, neon-like ions have a closed shell ground state configuration, $(1s^2 2s^2 2p^6)_{J=0}$, which makes them very stable and able to exist over a large electron-temperature range.

Unlike Kr^{34+} , the radiation from W^{64+} has not yet been investigated in a magnetic fusion plasma. Lower-charge neon-like ions between iron ($Z = 26$) and europium ($Z = 63$) have, however, been extensively investigated in the PLT tokamak [39–44] and the Alcator tokamak [45–48]. The core electron temperature in PLT routinely achieved values as high as 7 keV using lower hybrid radio frequency heating. These measurements have established a scaling for the electron temperature required for a given neon-like ion to start producing measurable L-shell line radiation [40]. Based on this scaling, neon-like tungsten is expected to be observable at an electron temperature of 12 keV or higher, as illustrated in figure 8.

In order to support the empirical scaling from PLT, we have made ionization balance calculations using the flexible atomic code (FAC) [49]. These calculations balanced electron-impact ionization (including both direct ionization and excitation autoionization contributions) and recombination rates (including radiative and dielectronic recombination processes). For L-shell ions, excitation autoionization included KL inner-shell excitations, and dielectronic recombination included KL, LL, and LM core excitation channels. For M-shell ions, excitation autoionization included LM inner-shell excitations, while dielectronic recombination included LM, MM and MN core excitation channels. The results are shown in figure 9. A

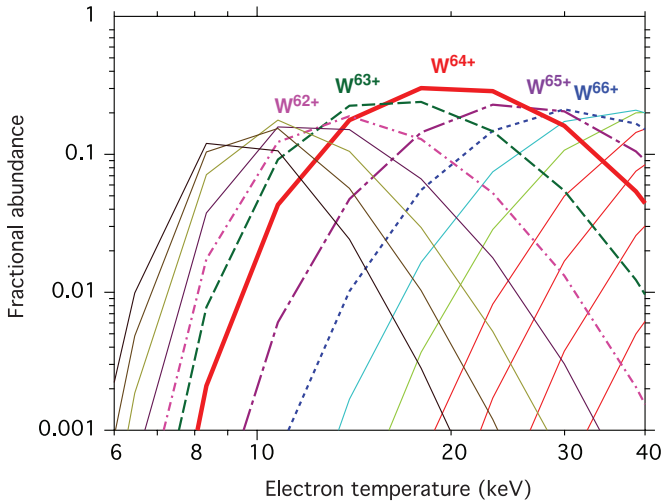


Figure 9. Predicted ionization balance of tungsten as a function of electron temperature showing the fractional ion abundances between W^{58+} and W^{72+} .

fractional abundance of W^{64+} ions of about 5% will likely be sufficient for detection, which means that the neon-like tungsten L-shell emission can serve as a diagnostic between 10 and 35 keV.

Predictions of the tungsten L-shell emission for an electron temperature of 18 and 30 keV made with the FAC are shown in figure 10. Neon-like tungsten has two strong sets of lines that may be used for ion temperature measurements. The first set consists of the two $3s \rightarrow 2p$ transitions just below 1.5 Å (around 8.3 keV). These lines are commonly labeled 3G and M2 [39] and correspond to the transitions from upper levels $(1s^2 2s^2 2p_{3/2}^5 3s_{1/2})_{J=1}$ and $(1s^2 2s^2 2p_{3/2}^5 3s_{1/2})_{J=2}$, respectively, to the closed-shell ground state. The second set comprises the $3d \rightarrow 2p$ transitions near 1.35 Å (around 9.1 keV), which are commonly labeled 3D and 3E [39]. These correspond to the transitions from upper levels $(1s^2 2s^2 2p_{3/2}^5 3d_{5/2})_{J=1}$ and $(1s^2 2s^2 2p_{3/2}^5 3d_{3/2})_{J=1}$, respectively, to the closed-shell ground state.

The region around the $3s \rightarrow 2p$ transitions is rather devoid of innershell satellite transitions, and it is attractive for exactly that reason. In other words, lines that may blend with and broaden lines 3G and M2 are weak, and determinations of the broadening or shift of the W^{64+} lines are relatively straightforward. The only complication arises from the predicted closeness of the two $3s \rightarrow 2p$ transitions. While the instrumental resolution is well able to resolve the two lines, the lines may blend with each other when the ion temperature reaches a certain value.

The region around the $3d \rightarrow 2p$ transitions is home to innershell satellite transitions from both lower and higher charge states of tungsten, as illustrated in figure 10. Although our calculations indicate that some weak transitions from neighbouring charge states blend with line 3D, none of the strong innershell satellite lines seem to blend with it. The exact wavelengths of these lines are still unknown, so that blending even with strong satellite lines is still a possibility. Moreover, at the predicted ion temperatures of 20–30 keV, the Doppler

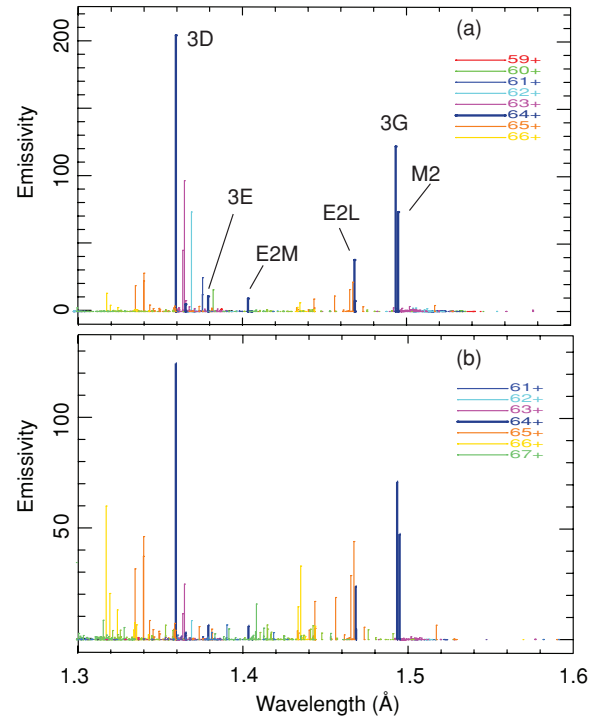


Figure 10. Predicted L-shell line emission from tungsten for electron temperatures of (a) 18 keV and (b) 30 keV. Only electron-impact excitation is included in the calculations. The neon-like W^{64+} lines are labeled in the notation of [40]. Here E2L and E2M denote the electric quadrupole transitions from upper levels $(1s^2 2s^2 2p_{3/2}^5 3p_{1/2})_{J=2}$ and $(1s^2 2s^2 2p_{3/2}^5 3p_{3/2})_{J=2}$, respectively, to the $(1s^2 2s^2 2p^6)_{J=0}$ ground state

broadening is so large that the intensity distributions from different spectral lines overlap, so that a detailed knowledge of the spectral lines in the neighbourhood of the line of interest for T_i measurements is absolutely necessary.

Our calculations only included electron-impact excitation and radiative cascades; they do not include dielectronic recombination. Dielectronic recombination results in dielectronic satellite transitions, which may also lead to line broadening and line shifts, as shown extensively for the x-ray spectra of helium-like ions [50–53]. These satellite lines have to be taken into consideration in analysing the spectra of helium-like ions, where they are very prominent and lead to apparent shifts and broadening that can overwhelm plasma effects, if not taken into account.

Calculations of the dielectronic recombination satellite lines were recently reported by Safronova *et al* both for satellites affecting the neon-like and the sodium-like tungsten lines [54, 55]. While some of these dielectronic satellite transitions blend with line 3D, they are generally rather weak and appear to be by far less of an issue than they are in helium-like spectra. The reduced size in the dielectronic satellite lines in neon-like ions has already been noted in the spectra observed on PLT [56]. However, full accounting of the satellite lines in the modelling spectra will be needed to correctly derive the ion temperature from the line shape and the ion velocity from the line centroid.

In the design of the CIXS we focus on the neon-like 3D line. It is predicted to be brighter than either of the two

$3s \rightarrow 2p$ transitions, and the surrounding innershell satellite lines will provide information on the ionization balance of the plasma. The latter may in turn give information on the electron temperature and transport properties of the plasma similar to the information provided by the K-shell spectra of helium-like ions [57]. Moreover, the ion temperature is expected to be about as large as the electron temperature (cf figure 2). This means that the two $3s \rightarrow 2p$ lines blend at temperatures where the W^{64+} abundance peaks, which would complicate analysis. This is illustrated in figures 11 and 12, where we show synthetic spectra of the tungsten L-shell emission calculated with FAC for electron temperatures between 5 and 40 keV. In order to produce spectra with a realistic line width, the ion temperature was set equal to the electron temperature. As a result, the line widths progressively broaden, as the electron temperature increases and as new emission from higher charge states is added to a given spectrum.

In figures 11 and 12 we have indicated the spectral region expected to be covered by the crystal spectrometer. By choosing the wavelength region covered by the spectrometer to include the transitions from several tungsten charge states lower than W^{64+} we can measure the ion temperature even in lower temperature plasmas where the neon-like emission is weak. Similarly, the emission from fluorine-like tungsten can be detected and utilized in very hot plasmas.

The choice of the tungsten L-shell radiation near the neon-like $3D$ transition has additional advantages over krypton. These advantages stem from the fact that the energy of the neon-like tungsten line is 4 keV lower than that of the resonance line of helium-like krypton. High-resolution ideal crystals, such as quartz or germanium, which are typically used for ion temperature diagnostics, have a much higher reflectivity for 9 keV lines than for 13 keV lines. For example, quartz ($\bar{5}145$) reflects the krypton K-shell lines near 42.3° , while quartz ($22\bar{4}3$) reflects the tungsten L-shell lines near 42.2° . Thus, both cuts satisfy the condition delineated in the preceding section that the Bragg angle should be $\leq 45^\circ$. The reflectivity of the ($22\bar{4}3$) cut for tungsten is, however, three times higher than that of the ($\bar{5}145$) cut for krypton. If germanium is used instead of quartz, the reflectivity of the cut required for tungsten will be almost five times higher than that for krypton. The comparison in crystal reflectivities for tungsten L-shell versus krypton K-shell radiation is listed in table 1. At the same time the quantum efficiency of typical x-ray detectors, such as the PILATUS-II detector used on the Alcator C-Mod tokamak [33, 58], is somewhat higher for the 9 keV tungsten lines than for the 13 keV krypton lines. This advantage, however, is compensated by the higher absorption losses experienced by the lower-energy x-rays in the vacuum windows made of beryllium, as tabulated in table 1.

Last but not least, tungsten has another great advantage over krypton. At an electron temperature of 25 keV and a density of 10^{14} cm^{-3} , each W^{64+} ion emits eight times more photons than a helium-like Kr^{34+} ion. Specifically, using FAC we calculate an emissivity of $730 \text{ photons s}^{-1}$ for each W^{64+} ion in the line of interest, i.e., line $3D$. This compares to $92 \text{ photons s}^{-1}$ for each Kr^{34+} ion in the heliumlike resonance line.

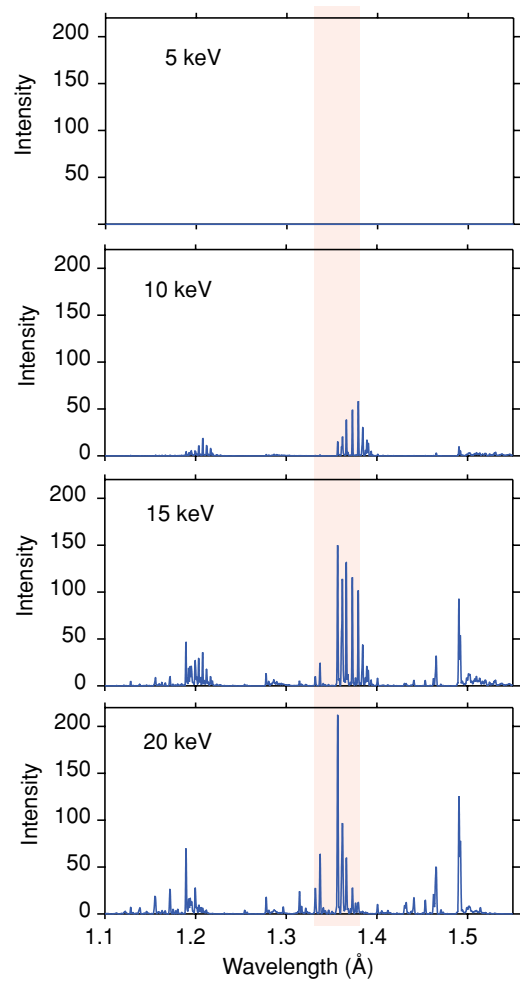


Figure 11. Predicted L-shell line emission from tungsten for electron temperatures of 5, 10, 15, and 20 keV. The shaded area indicates the wavelength region covered by the ITER x-ray crystal spectrometer.

When taking into account all factors listed in table 1, we obtain about 25–40 times higher throughput for an ITER crystal spectrometer based on tungsten than an instrument based on krypton. A higher x-ray count rate translates to higher temporal resolution, which is essential for making the best measurements possible. Alternatively, the tungsten concentration can be much lower than would be needed to get an equivalent count rate for krypton. In fact, using tungsten rather than krypton means that the radiative power losses from ITER plasmas are considerably reduced, even if both had to be injected into the plasma. (Tungsten can be injected into the plasma, for example, in the form of tungsten hexacarbonyl, $W(CO_2)_6$.) Although the overall radiative power loss due to tungsten is about 6 to 10 times larger per ion than due to krypton [29], the fact that 25–40 times fewer tungsten ions are needed than krypton ions means that the overall radiation losses are smaller. Based on the calculations for krypton [59], we estimate a radiative power loss of about 1 MW, which is very reasonable.

As we mentioned earlier, the current predictions place the tungsten concentration in ITER plasmas at around 10^{-5} . Our CIXS design incorporates a crystal that is 50 mm wide and

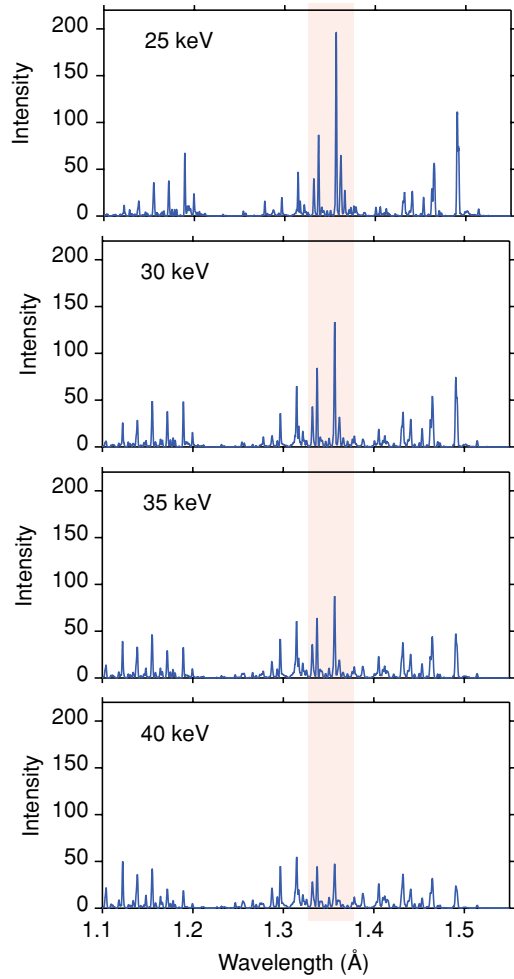


Figure 12. Predicted L-shell line emission from tungsten for electron temperatures of 25, 30, 35, and 40 keV. The shaded area indicates the wavelength region covered by the ITER x-ray crystal spectrometer.

Table 1. Comparison of the instrumental and atomic physics quantities associated with using the K-shell radiation of Kr^{34+} and the L-shell radiation of W^{64+} ions.

Quantity	Kr^{34+}	W^{64+}
X-ray energy	13.1	9.1
Accessible T_e range	7–30 keV	10–35 keV
Detector quantum efficiency	70%	90%
Window (1 mm Be) transmissivity	94%	87%
Quartz crystal cut	($\bar{5}145$)	($22\bar{4}3$)
Quartz Bragg angle	42.3°	42.2°
Quartz reflectivity	$1.4 \mu\text{rad}$	$4.3 \mu\text{rad}$
Ge crystal cut	(555)	(440)
Ge Bragg angle	46.4°	42.8°
Ge reflectivity	$4.0 \mu\text{rad}$	$19.2 \mu\text{rad}$
Emissivity (25 keV, 10^{14} cm^{-3})	92 photons/s/ion	730 photons/s/ion

13 mm tall and utilizes a PILATUS-II detector. In that case we estimate that 10^7 photons strike each spatial resolution element per second. Even if that number is reduced by a factor of 10, i.e. if the tungsten concentration is at 10^{-6} , which

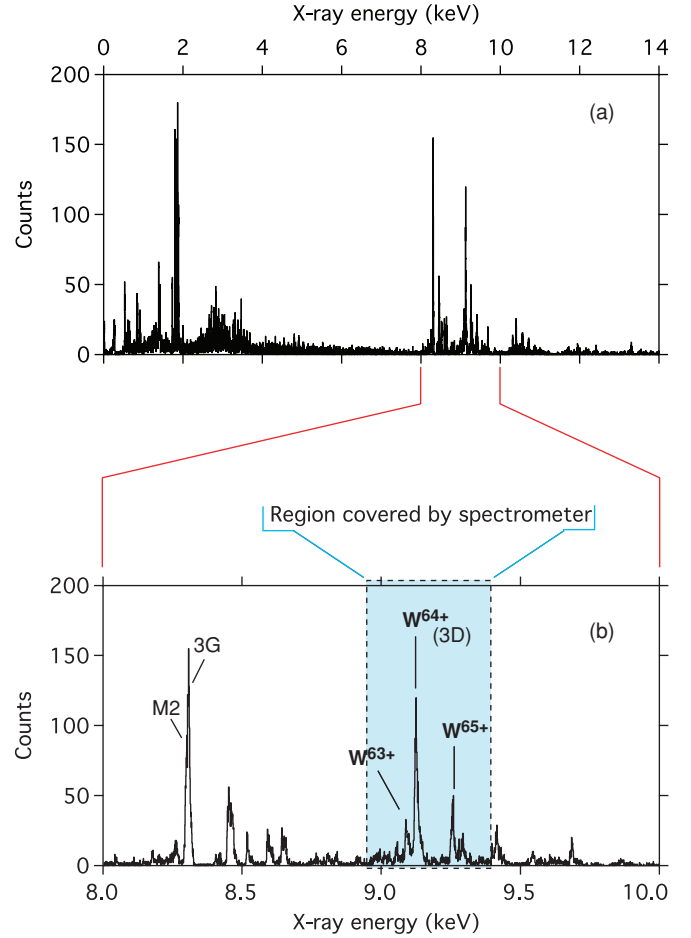


Figure 13. X-ray emission from tungsten measured with the EBIT calorimeter spectrometer (ECS) at the Livermore SuperEBIT electron beam ion trap: (a) full region covered by the ECS; (b) blow-up of the region near lines $M2$, $3G$ and $3D$. The shaded area indicates the wavelength region covered by the ITER crystal spectrometer. The electron beam energy for the measurement was 23 keV.

is much lower than assumed for ITER, the count rate in the tungsten $3D$ line is still around a million per second per spatial resolution element, which is sufficient to have a time resolution of one millisecond per spatial point.

5. Laboratory data on L-shell tungsten

The atomic data needed for understanding the neon-like tungsten spectrum is still rather uncertain and mostly only known from calculations. On the other hand, this situation is not too much different from how well the atomic data are known associated with the spectrum of helium-like krypton.

Lines from neon-like tungsten and above have been measured in preliminary fashion on the Livermore EBIT-I and SuperEBIT electron beam ion traps [60, 61], which is one of the few devices world-wide which can produce the radiation of such a highly charged ion. Preliminary measurements have also been reported by the Berlin EBIT group [62].

A spectrum of tungsten obtained with the EBIT calorimeter spectrometer (ECS) on the Livermore SuperEBIT

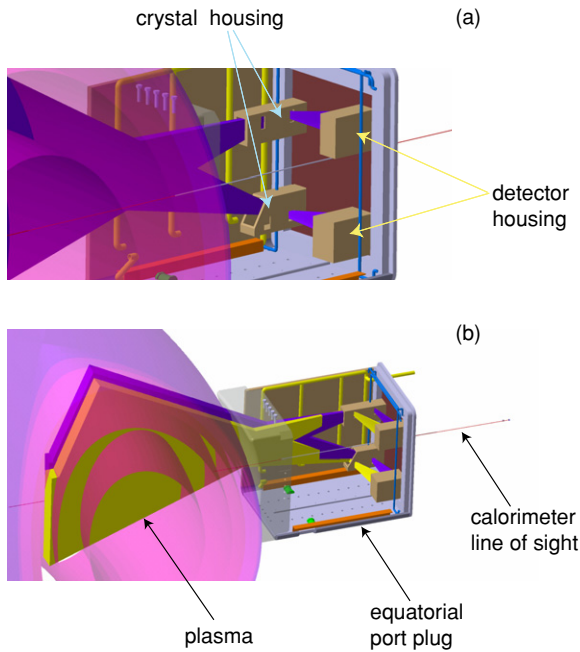


Figure 14. Conceptual design of the core imaging x-ray spectrometer: (a) radial view only, (b) radial and toroidal view. Also shown is the line of sight for an x-ray calorimeter.

device is shown in figure 13. The ECS has a resolution of about 5 eV across the entire spectral band recorded by the instrument (0.1 – 15 keV) [63, 64]. This spectrum, therefore, not only shows the $3 \rightarrow 2$ lines, but also the $2 \rightarrow 2$ and $4 \rightarrow 3$ lines, among many other transitions seen. A blow-up of the spectrum in figure 13(b) shows the innershell satellite lines, which are close to the neon-like $3D$ line. The 5 eV resolution of the ECS is equivalent to line broadening caused by the Doppler motion of the tungsten ions in a roughly 8 keV plasma. This means that the lines will be even less resolved in an ITER spectrum, where the ion temperature may easily be two, three, or four times as high. Knowing the exact position of these innershell satellite lines will thus be critical for determining the broadening and shift of line $3D$ from the spectral observations.

The effect of dielectronic satellite lines on the apparent broadening and shift of the dominant K-shell helium-like lines was understood fully only recently [65]. By comparison, little experimental data are available on neon-like ions. Measurements on the Berlin and Tokyo electron beam ion traps have recently considered dielectronic recombination rates [66, 67]. However, detailed experiments will be needed to understand the location and behaviour of the dielectronic satellite lines with electron temperature at the specific location of the neon-like tungsten lines. Fortunately, investigation of dielectronic satellite lines of lower- Z neon-like ions have found them to be rather weak [56], especially when compared to the dielectronic satellite lines in helium-like ions, which are very strong at low plasma temperature.

6. Spectrometer layout on ITER

The CIXS on ITER will need to provide a radial profile of the ion temperature and of the toroidal ion velocity. To accomplish

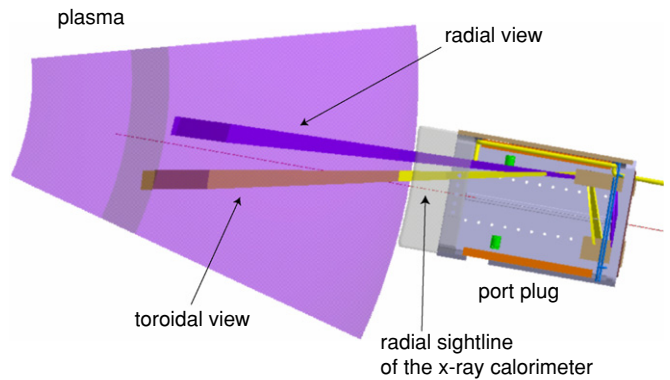


Figure 15. Conceptual design of the core imaging x-ray spectrometer (top view). The radial and toroidal views are shown in blue and yellow, respectively. The line of sight for an x-ray calorimeter is also indicated.

this task the spectrometer ideally will need to have a full view of the plasma. A full view will give constraints for establishing the radial profile from the inversion of the data obtained from the different plasma chords. Furthermore, there needs to be one set of sight lines viewing the plasma in a radial fashion, from which the ion temperature and possibly the poloidal rotation can be inferred, and another set viewing the plasma at an angle, from which the toroidal motion can be derived.

Practical considerations have placed specific constraints on the instrument design. First, the instrument must fit into one of the equatorial port plugs on ITER, as mentioned earlier. The designated plug for the CIXS is shared with the US Electron Cyclotron Emission diagnostic, the US Toroidal Interferometer Polarimeter diagnostic, and the EU Visible/Infrared Imaging System. Moreover, the viewing slot can only have a certain length, which limits the fraction of the plasma that can be seen.

Working within the constraints imposed by the port plug geometry and the space envelopes of co-located diagnostics has produced an instrument design that provides both a radial and a toroidal view of the core of the plasma and much of its surrounding region. The radial view requires a set of two crystals and two associated detector arrays, as shown in figure 14(a). The set produces overlapping views of the plasma centre. The first crystal is placed on a plane parallel to the horizontal midplane of the plasma and views the plasma core. The second crystal is placed well below the first, and it views the plasma above the core. Both crystals use the same slot in the blanket shield module (which is the interface between the interior of the vessel and the port plug) in order to eliminate the need for a second slot. The toroidal view is accomplished the same way as the radial view, except that the crystals in this case are located somewhat forward compared to the location of the crystals providing the radial view, as shown in figure 14(b). This has the effect of a counterclockwise rotation by about 10° of the crystal-detector arrangement when viewed from above. This rotation is needed in order to pick up a toroidal velocity component. The top view of the instrument is illustrated in figure 15.

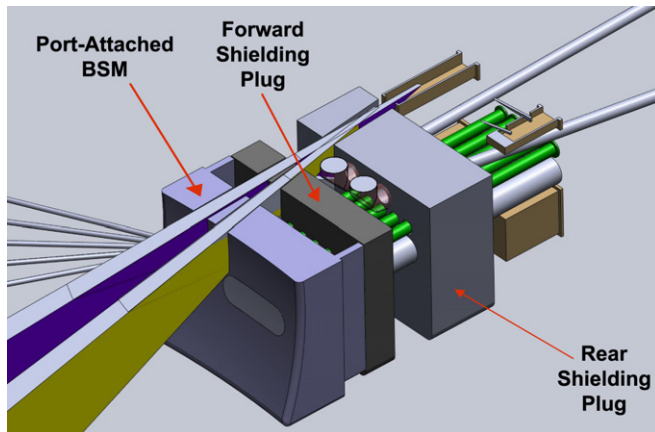


Figure 16. Conceptual design of the diagnostic layout in equatorial port plug 9, which houses several diagnostics, including the visible/IR camera, the electron cyclotron emission system, the toroidal interferometer polarimeter, and the core imaging x-ray spectrometer. The slots needed for both the radial and toroidal views in the blanket shield module (BSM) are shown.

We note that for both views the detectors are located on the back wall of the port plug. That has the great advantage that the detectors can be serviced by removing the detector module via a flange on the back of the port plug.

Both figures 14 and 15 present the CIXS in an empty port plug for better illustration of the spectrometer geometries. In figure 16 we show the layout of the port plug that includes the components of the other instrumentation. Any leftover space is filled with shielding.

7. Conclusion

The ITER environment is highly challenging for the development of plasma diagnostics. The plasmas will be hotter and bigger than ever before, which requires instrumentation that is quite different from what has been utilized at other machines. In addition, any diagnostic within one of the port plugs must deal with a high neutron environment and be able to handle a bakeout temperature between 200° and 300 °C.

Our design for measuring the core ion temperature and bulk toroidal and poloidal ion velocity departs from early designs, which employed cylindrically bent crystals and single lines of sight through the plasma. Our new instrument employs spherically bent crystals, which enable plasma imaging. Moreover, the new instrument is based on the L-shell emission of neon-like tungsten instead of the K-shell emission from a high-Z helium-like element, such as krypton.

The CIXS instrument is currently designed to study ion temperatures above about 10 keV. Core plasma temperatures below 10 keV are expected when ITER is operated without auxiliary heating systems. Design studies are currently under way to identify options to measure temperatures below that limit when neon-like tungsten is not produced. A potential intrinsic impurity, which might be used in this case, is iron.

As with any diagnostic that has not yet been operated under harsh ITER-like conditions, there are risks that can limit successful operation of the CIXS. Risk mitigation

may include the use of an x-ray calorimeter array on ITER. X-ray calorimeter arrays have been used successfully on the Livermore EBIT-I and SuperEBIT devices since 2000 (cf figure 13) and are now in the third generation, while the implementation of the fourth-generation array is expected for 2010 [63]. Originally developed as space flight instrumentation, the devices have been successfully used in rocket flights and on the Suzaku satellite mission [68, 69]. The next generation arrays, which will become available in a few years and well before ITER plasma startup, will have a resolution of 2 eV and >1000 detector elements.

In a preliminary study, we have determined that an x-ray calorimeter requires minimal port space (roughly a 2.5 cm inner-diameter vacuum tube, cf figures 14 and 15), and the actual detector and electronics could be located outside the biological shield, i.e. tens of meters away from the plasma.

The resolving power of a calorimeter (even those built in 2007) is high enough to determine the core ion temperature from the line shape of the tungsten L-shell radiation. Moreover, while crystal spectrometers cover only a very small spectral range, calorimeters would cover the entire spectral band between about 0.2 and 15 keV, including the bremsstrahlung background and free-bound continuum emission (cf figure 13). Thus, the calorimeter would provide information on the electron temperature and impurity concentration. The latter is very important to assess how strong the tungsten L-shell radiation is in ITER, especially, if it should drop to a point below which it can no longer be detected with the crystal spectrometer. A 1000-pixel calorimeter can perform these measurements with moderate time resolution (roughly 100–500 ms). The calorimeter detector could thus serve as a backup for core ion temperature measurements and would provide valuable data in addition to the ion temperature along its line of sight.

A conceptual design review of the CIXS is planned for 2010. This will be a crucial step for finalizing the conceptual design and for starting the construction of the instrument, in order to have it available when the first plasmas are produced with ITER.

Acknowledgments

This work was performed under the auspices of the US Department of Energy by Lawrence Livermore National Laboratory under contract DE-AC52-07NA27344.

References

- [1] Paerels F B S and Kahn S M 2003 *Annu. Rev. Astron. Astrophys.* **41** 291
- [2] de Michelis C and Mattioli M 1981 *Nucl. Fusion* **21** 677
- [3] Stratton B C, Bitter M, Hill K W, Hillis D L and Hogan J T 2008 *Fusion Sci. Technol.* **53** 431
- [4] von Goeler S, Stodiek W, Eubank H, Fishman H, Grebenshchikov S and Hinnov E 1975 *Nucl. Fusion* **15** 301
- [5] Bitter M, von Goeler S, Horton R, Goldman M, Hill K, Sauthoff N R and Stodiek W 1979 *Phys. Rev. Lett.* **42** 304
- [6] Platz P, Ramette J, Belin E, Bonnelle C and Gabriel A 1981 *J. Phys. E* **14** 448
- [7] Källne E, Källne J and Rice J E 1982 *Phys. Rev. Lett.* **49** 330

- [8] Apicella M L, Bartiromo R, Bombarda F and Giannella R 1983 *Phys. Lett.* **98A** 174
- [9] TFR Group, Cornille M, Dubau J and Loulergue M 1985 *Phys. Rev. A* **32** 3000
- [10] Lee P, Lieber A J, Pradhan A K and Xu Y 1986 *Phys. Rev. A* **34** 3210
- [11] Hsuan H, Bitter M, Hill K W, von Goeler S, Grek B, Johnson D, Bhalla C P, Karim K R, Bely-Dubau F and Faucher P 1987 *Phys. Rev. A* **35** 4280
- [12] Bombarda F, Giannella R, Källne E, Tallents G J, Bely-Dubau F, Faucher P, Cornille M, Dubau J and Gabriel A H 1988 *Phys. Rev. A* **37** 504
- [13] Zastrow K-D, Källne E and Summers H P 1990 *Phys. Rev. A* **41** 1427
- [14] Schumacher U, Barnsley R, Fußmann G, Assmussen K, Chu C C and Janeschitz G 1992 *Atomic Processes in Plasmas (AIP Conf. Proc. no 257)* (New York: AIP) p 131
- [15] Bitter M, Hsuan H, Rice J E, Hill K W, Diesso M, Grek B, Hulse R, Johnson D W, Johnson L C and von Goeler S 1988 *Rev. Sci. Instrum.* **59** 2131
- [16] Rice J E, Bombarda F, Graf M A, Marmar E S and Wang Y 1995 *Rev. Sci. Instrum.* **66** 752
- [17] Fonck R J and Hulse R A 1984 *Phys. Rev. Lett.* **52** 530
- [18] Schilling G and Synakowski E J 1992 *Rev. Sci. Instrum.* **63** 4937
- [19] Thomas D M, Burrell K H, Snider R T and Wade M R 1999 *Rev. Sci. Instrum.* **70** 886
- [20] Donné A J H, Barnsley R and von Hellermann M G 2008 *Spectral Line Shapes, Vol. 15: 19th Int. Conf. (American Institute of Physics Conference Series Vol. CP1058)* ed M A Gigos and M Á Gonzáles (New York: AIP) p 195
- [21] Schunke B, Bora D, Antoni V, Bonicelli T, Chakraborty A, Cordier J-J, Hemsworth R, Inoue T, Tanga A and Watanabe K 2008 *Plasma and Fusion Science (American Institute of Physics Conference Series vol CP996)* ed C Varandas and C Silva (New York: AIP) p 34
- [22] Donné A J H *et al* and the ITPA Topical Group on Diagnostics 2007 *Nucl. Fusion* **47** S337
- [23] Sugie T, Costley A, Malaquias A and Walker C 2003 *J. Plasma Fusion Res.* **79** 1051
- [24] Barnsley R, Mullane M G O, Ingesson L C and Malquias A 2004 *Rev. Sci. Instrum.* **75** 3743
- [25] Bitter M, Hill K W, Roquemore A L, Beiersdorfer P, Kahn S M, Elliott S R and Fraenkel B 1999 *Rev. Sci. Instrum.* **70** 292
- [26] Shimada M 2004 Plasma Performance Assessment—August 2004, *ITER report 27SZNW v1.0*
- [27] Peacock N J, Mullane M G O, Barnsley R and Tarbutt M R 2008 *Can. J. Phys.* **86** 277
- [28] Skinner C H 2008 *Can. J. Phys.* **86** 285
- [29] ITER Physics Expert Group on Divertor, ITER Physics Expert Group on Modelling and Database, and ITER Physics Basic Editors 1999 *Nucl. Fus.* **39** 2391
- [30] Johann H H 1931 *Z. Phys.* **69** 185
- [31] Hámos L v 1933 *Ann. der Phys.* **17** 716
- [32] Bitter M *et al* 2004 *Rev. Sci. Instrum.* **75** 3660
- [33] Ince-Cushman A *et al* 2008 *Rev. Sci. Instrum.* **79** 100000
- [34] Beiersdorfer P *et al* 1995 *Atomic Processes in Plasmas (AIP Conf. Proc. No. 322)* ed W L Rowan (New York: AIP) p 129
- [35] Widmann K, Beiersdorfer P, Decaux V, Elliott S R, Knapp D, Osterheld A, Bitter M and Smith A 1995 *Rev. Sci. Instrum.* **66** 761
- [36] Widmann K, Beiersdorfer P, Decaux V and Bitter M 1996 *Phys. Rev. A* **53** 2200
- [37] Bitter M *et al* 1993 *Phys. Rev. Lett.* **71** 1007
- [38] Bitter M, Hsuan H, Hill K W, R. Hulse, Zarnstorff M and Beiersdorfer P 1993 *Atomic and Plasma-Material Interaction Processes in Controlled Thermonuclear Fusion* ed R K Janev and H W Drawin (Amsterdam: Elsevier) p 119
- [39] Beiersdorfer P, Bitter M, von Goeler S, Cohen S, Hill K W, Timberlake J, Walling R S, Chen M H, Hagelstein P L and Scofield J H 1986 *Phys. Rev. A* **34** 1297
- [40] Beiersdorfer P *et al* 1988 *Phys. Rev. A* **37** 4153
- [41] Nilsen J *et al* 1994 *Phys. Rev. A* **50** 2143
- [42] Beiersdorfer P, Nilsen J, Scofield J, Bitter M, von Goeler S and Hill K W 1995 *Phys. Scripta* **51** 322
- [43] Beiersdorfer P, von Goeler S, Bitter M and Thorn D B 2001 *Phys. Rev. A* **64** 032705
- [44] Beiersdorfer P, Bitter M, von Goeler S and Hill K W 2004 *Astrophys. J.* **610** 616
- [45] Källne E, Källne J and Cowan R D 1983 *Phys. Rev. A* **27** 2682
- [46] Rice J E, Fournier K B, Graf M A, Terry L, Finkenthal M, Bombarda F, Marmar E S and Goldstein W H 1995 *Phys. Rev. A* **51** 3551
- [47] Rice J E, Fournier K B, Terry J L, Graf M A, Finkenthal M, Marmar E S and Goldstein W H 1996 *Phys. Rev. A* **53** 3953
- [48] Rice J E, Fournier K B, Goetz J A, Marmar E S and Terry J L 2000 *J. Phys. B: At. Mol. Opt. Phys.* **33** 5435
- [49] Gu M F 2008 *Can. J. Phys.* **86** 191
- [50] Bitter M, Hill K W, Sauthoff N R, Efthimion P C, Merservey E, Roney W, von Goeler S, Horton R, Goldman M and Stodiek W 1979 *Phys. Rev. Lett.* **43** 129
- [51] Bitter M, von Goeler S, Hill K W, Horton R, Johnson D, Roney W, Sauthoff N, Silver E and Stodiek W 1981 *Phys. Rev. Lett.* **47** 921
- [52] Schneider P, Beiersdorfer M B, Bitter M and von Goeler S 1992 *Rev. Sci. Instrum.* **63** 5029
- [53] Smith A J, Beiersdorfer P, Decaux V, Widmann K, Reed K J and Chen M H 1996 *Phys. Rev. A* **54** 462
- [54] Safronova U I, Safronova A S and Beiersdorfer P 2009 *J. Phys. B: At. Mol. Opt. Phys.* **42** 165010
- [55] Safronova U I, Safronova A S and Beiersdorfer P 2009 *At. Data Nucl. Data Tables* **95** 751
- [56] Beiersdorfer P 1988 *PhD Thesis*, Princeton University
- [57] Bitter M, von Goeler S, Sauthoff N, Hill K, Brau K, Eames D, Goldman M, Silver E and Stodiek W 1981 *Int. Conf. X-ray Processes and Inner-Shell Ionization (Stirling, UK, 1980)* ed D J Fabian, H Kleinpoppen and L M Watson (New York: Plenum) p 861
- [58] Hill K W *et al* 2008 *Rev. Sci. Instrum.* **79** 100000
- [59] Ingesson L C, Barnsley R, Malquias A and Mullane M G O 2004 *Rev. Sci. Instrum.* **75** 3696
- [60] Beiersdorfer P 1993 *VIth Int. Conf. Physics of Highly Charged Ions (AIP Conf. Proc. No. 274)* ed P Richard, M Stöckli, C L Cocke and C D Lin (New York: AIP) p 365
- [61] Podpaly Y, Clementson J, Beiersdorfer P, Williamson J, Brown G V and Gu M F 2009 *Phys. Rev. A* **80** 052504
- [62] Biedermann C, Radtke R, Seidel R and Pütterich T 2009 *Phys. Scr.* **T134** 014026
- [63] Porter F S *et al* 2008 *Can. J. Phys.* **86** 231
- [64] Porter F S, Beiersdorfer P, Brown G V, Doriese W, Kelley R L, Kilbourne C A, King J, Irwin K, Reintsema C and Ullom J 2008 *J. Low Temp. Phys.* **86** 231
- [65] Bitter M *et al* 2003 *Phys. Rev. Lett.* **91** 265001
- [66] Watanabe H, Nakamura N, Kato D, Nakano T and Ohtani S 2007 *Plasma Fusion Res. Rapid Commun.* **2** 027
- [67] Biedermann C, Radtke R, Seidel R and Behar E 2009 *J. Phys. Conf. Ser.* **163** 012034
- [68] Stahle C K, McCammon D and Irwin K D 1999 *Phys. Today* **52** 32
- [69] Kelley R L *et al* 2007 *Pubs. Astron. Soc. Japan* **59** 77